Journal of Hazardous Materials 424 (2022) 127353

Contents lists available at ScienceDirect

Journal of Hazardous Materials

journal homepage: www.elsevier.com/locate/jhazmat

Research paper

Nano-sized zeolite-like metal-organic frameworks induced hematological effects on red blood cell

Fang Hao [a,b,d], Xiu-Ping Yan [a,b,c,d,*]

[a] State Key Laboratory of Food Science and Technology, Jiangnan University, Wuxi 214122, China
[b] International Joint Laboratory on Food Safety, Jiangnan University, Wuxi 214122, China
[c] Key Laboratory of Synthetic and Biological Colloids, Ministry of Education, Jiangnan University, Wuxi 214122, China
[d] Institute of Analytical Food Safety, School of Food Science and Technology, Jiangnan University, Wuxi 214122, China

ARTICLE INFO

Editor: Dr. S Nan

Keywords:
Metal organic framework
Hematotoxicity
Mechanism of hemolysis
Hemoglobin
Bioconjugation

ABSTRACT

Understanding the toxicity of metal-organic frameworks (MOFs) is important for improving their biocompatibility in further applications, especially the hematotoxicity of MOFs due to the unavoidable contact of MOFs with blood in biomedical science. Here we report the hematotoxicity and underlying mechanisms of nano-sized zeolite-like MOFs ZIF-8 and ZIF-67 because of their wide applications in biomedical science. ZIF-67 induced significant hemolysis of red blood cell (Rb) through breaking the structure of membrane due to the generation of free radicals, whereas ZIF-8 was hematocompatible. ZIF-67 was thus internalized by Rb and then bound with hemoglobin via hydrogen bond and van der Waals force, which influenced the structure and function of hemoglobin in accompany with heme release. These findings reveal the detailed mechanism of the hematological effects of MOFs on Rb and are helpful to the assessment of the toxicity and potential health risks of MOFs and the design of biosafe MOFs for biomedical applications.

1. Introduction

Metal organic frameworks (MOFs) are a new kind of microporous crystalline materials composed of metal ions or clusters and organic linkers, which are connected via coordination bonds (Gu et al., 2012; Kreno et al., 2012; Li et al., 1999). Nano-sized MOFs have received great interests in biomedical applications, such as biosensing, bioimaging, and drug delivery due to their high porosity, large specific surface area, tunable channel structure and easy functionalization (Riccò et al., 2018; Furukawa et al., 2015; Simon-Yarza et al., 2018). Zeolite-like MOFs (ZMOFs), an important kind of MOFs with zeolite-like structure, are promising materials for the construction of theranostic nanoplatforms as ZMOFs can load multiple kinds of guest molecules (e.g., proteins, drugs, etc.) via one-pot synthesis and degrade with controllable way in cellular acidic condition to release guest cargoes, which endows ZMOFs with outstanding characters of pharmacokinetics (Deng et al., 2019; Chen et al., 2018; Feng et al., 2019). For instance, ZIF-8 was used to encapsulate doxorubicin for delivery to tumor and degrade for cancer therapy or imaging (Carrillo et al., 2019; Hao et al., 2019; Yan et al., 2020). ZIF-67 was explored to carry drug and generate hydroxyl radicals for synergetic killing of cancer cells (Gao et al., 2019; Sang et al., 2020). In these applications, ZMOFs are mainly administrated into blood circulation to transmit to focal sites. Therefore, the hematotoxicity of such ZMOFs should be evaluated to avoid potential adverse effects.

Recent in vitro and in vivo studies revealed that several physiochemical factors of MOFs, such as size, surface modification, and metal species have effects on the toxicological activity of MOFs (Kumar et al., 2019). NH_2-functionalized UiO-66 gave stronger toxicological effect on HepG2 cells and zebrafish embryos than bare UiO-66 (Ruyra et al., 2015). Fe-based MOF MIL-100 was more cytotoxic to cancer cells than Zn-based MOF ZIF-8 (Tamames-Tabar et al., 2014), while ZIF-8 exhibited higher cellular toxicity than Cu-based MOF MIL-160 in the same concentration range (Wagner et al., 2019). An in vivo study showed that the large size of ZIF-67 (890 nm) made more significant damage to rat neuron system than small ones (60 nm) (Deng et al., 2021). Polyethylene glycol (PEG)-functionalized Fe-based MOF MIL-88A gave less hepatic change of rat than bare MIL-88A (Horcajada et al., 2010). Additionally, both Cu- and Eu-based MOFs were non-toxic to zebrafish and adult rats at 1.5 μg/mL and 300 mg/kg, respectively (Lucena et al., 2017; Abramenko et al., 2021). Nevertheless, the hematotoxicity of different metal-based ZMOFs is still unclear.

The interaction of red blood cell (Rb) and nanoparticles (NPs) could

* Corresponding author at: State Key Laboratory of Food Science and Technology, Jiangnan University, Wuxi 214122, China.
E-mail address: xpyan@jiangnan.edu.cn (X.-P. Yan).

https://doi.org/10.1016/j.jhazmat.2021.127353
Received 12 August 2021; Received in revised form 21 September 2021; Accepted 23 September 2021
Available online 28 September 2021

make toxic effects on Rb such as shape deformation, hemolysis, and thrombus formation (de la Harpe et al., 2019). Large quantum dots (LQDs) was found more hematotoxic than small ones (SQDs) as the hemolysis ratio of LQDs was higher than that of SQDs (Wang and Jiang, 2015). The shape of NPs also influenced the hemolysis and the rod-like silica NPs were more toxic than spherical ones (Ma et al., 2014). Positively charged gold nanorods induced hemolysis while negatively charged gold nanorods were hemocompatible (Zhao et al., 2017).

Hemoglobin is the most abundant protein in Rb and exerts many physiological functions in erythrocytes (Giardina et al., 1995). The hemoglobin released from Rb after hemolysis would be adsorbed by NPs and its structure and function may be compromised, which exhibited hematotoxic fate at biomolecular level (Li et al., 2014; Jun et al., 2011). However, the hematotoxicity effects induced by MOFs are still unclear, which hinders the understanding of the potential risks of MOFs.

There are many factors that determine the toxicity of metal-based nanoparticles. Predicting their toxicity only based on the corresponding metal ions is not reliable. For instance, ZnO nanoparticles are more toxic than Ag nanoparticle at the same concentration though Ag ion is more toxic than Zn ion (Kang et al., 2015). Moreover, Zn-based ZIF-8 exhibited higher cytotoxicity than Cu-based MIL-160 in the same concentration range though Cu ion is more toxic than Zn ion (Wagner et al., 2019). These previous results indicate the great necessity for the study on the toxicity and the underlying mechanisms of metal-based nanoparticles.

Herein, we show the hematological effect of nanosized ZMOFs and the underlying mechanisms. We take ZIF-8 and ZIF-67 as model ZMOFs because they have recently received great attention in diverse fields for their unique structures and properties (Gao et al., 2021; Freund et al., 2021; Feng et al., 2016). ZIF-8 and ZIF-67 exhibit a sodalite-related zeolite type structure and large pores that are accessible through small pore windows with the same ligand 2-methylmidazole as the linker, but different metal ions (Zn^{2+} and Co^{2+} in ZIF-8 and ZIF-67, respectively) as the coordination center (Banerjee et al., 2008; Park et al., 2006). Different metal ions in ZIF-8 and ZIF-67 result in remarkable difference in hematotoxicity. ZIF-8 is hematocompatible whereas ZIF-67 is considerably hematotoxical. The mechanisms for such big differences in hematotoxicity for ZIF-8 and ZIF-67 are studied in detail. This work provides robust clues on the potential health risk of nano-sized ZMOFs to guide their environmental toxicity study for further biomedical applications.

2. Experimental section

2.1. Chemicals

$Zn(NO_3)_2{\cdot}6H_2O$, $Co(NO_3)_2{\cdot}6H_2O$, 2-methylimidazole (2-MI), dimethyl sulfoxide (DMSO), nitrotetrazolium blue chloride (NBT), terephthalic acid (TPA), PEG600, PEG2000, urea, methanol, chloroform and ammonium acetate were from Sinopharm Chemical Reagent Co. Ltd. (Shanghai, China). Phosphate buffer saline (PBS) (6.7 mM, pH 7.4) was from Hyclone Co. Ltd. (USA). 3,3′-dioctadecyloxacarbocyanine perchlorate (DiO), 2,7-dichlorodi-hydrofluorescein diacetate (DCFH-DA), bicinchoninic acid (BCA) kit, and lysis solution of radio immunoprecipitation assay (RIPA) were from Thermo Fisher Scientific Co. Ltd. (USA). Hemoglobin was from Sigma Aldrich Co. Ltd. (China). All the other reagents were from Aladdin Chemistry Co. Ltd. (Shanghai, China) unless otherwise stated.

2.2. Synthesis of ZIFs

ZIF-8 and ZIF-67 were prepared according to Feng et al (Freund et al., 2021). Briefly, 0.66 g 2-MI, 0.30 g $Zn(NO_3)_2{\cdot}6\ H_2O$ (for synthesis of ZIF-8) or 0.30 g $Co(NO_3)_2{\cdot}6\ H_2O$ (for synthesis of ZIF-67), and 4 mL DMSO were mixed and stirred at room temperature for 20 min. The ZIF-8 and ZIF-67 were purified by centrifugation (11,363 g, 15 min) and DMSO washing (three times). Final stocking solutions were maintained in DMSO at room temperature. The ZIF-8 and ZIF-67 were washed with ultrapure water (three times) before use. The molar concentrations of ZIF-8 and ZIF-67 were obtained on a Nanoparticle Tracking Analysis (NTA, NS300, Malvern, UK).

2.3. Rb labelling and imaging

Rb (2×10^6/mL) was incubated with 1 μM DiO for 15 min and washed with PBS to remove the excessive DiO. The as-prepared Rb was incubated with PBS (negative control), ultrapure water (positive control), and ZIF-8/67 (0.9 and 7.5 nM in PBS) for 10 min. After washing with PBS, Rb was dropped onto a coverslip and pictured on a Laser scanning confocal microscopy (LSCM, FV3000, Olympus, Japan) in the emission wavelength range of 500–650 nm under excitation at 488 nm with a 60 × objective.

2.4. Hemolysis assay

Whole blood (WB, 10%, v:v) or Rb (2×10^6/mL) was incubated with different concentrations of ZIF-8 and ZIF-67 (0.9, 1.8, 3.7, 7.5, 15, and 30 nM in PBS) for 10 min. The supernatant was isolated by centrifugation and its absorbance was measured on a UV-3600 spectrophotometer (SHIMAZU, Japan) at 541 nm. The percentage of hemolysis was calculated according to a previous study (Dobrovolskaia et al., 2008). As for time-course of hemolysis measurement, the ZIF-8 and ZIF-67 (7.5 nM in PBS) were added into Rb solution and the supernatant was isolated for absorbance detection at 10, 30, 60, 120, and 180 min

2.5. Reactive oxygen species (ROS) detection

The ROS produced by ZIF-8 and ZIF-67 was detected with spectral method. For total ROS detection, DCFH-DA (100 μM) was incubated with different concentrations of ZIF-8 and ZIF-67 (0.9, 1.8, 3.7, 7.5, and 15 nM in PBS) for 20 min. Then, the supernatant was isolated by centrifugation (11,363 g, 20 min) for fluorescence measurement on a multiplate reader (Synergy H1, Biotek, USA) with $\lambda_{ex}/\lambda_{em}$ at 485/530 nm. 10 mM H_2O_2 and ultrapure water were used as positive control and negative control, respectively. The results were expressed as relative fluorescent intensity compared to negative control.

NBT was used for $O_2^{\bullet-}$ detection. The mixture of NBT (75 μM) and ZIF-67 (0.9, 1.8, 3.7, 7.5 nM in PBS) was maintained at room temperature for 20 min without light irradiation. The supernatant was isolated by centrifugation (11,363 g, 20 min) and UV–vis spectra (UV-3600, SHIMAZU, Japan) were measured from 400 nm to 800 nm. The mixture containing riboflavin (20 μM) and methionine (13 mM) illuminated by UV lamp for 20 min was used as positive control.

TPA fluorescence method was used to detect •OH. The solution in experimental group containing TPA (20 μM) and ZIF-67 (0.9, 1.8, 3.7, 7.5 nM in PBS) was incubated for 20 min and the supernatant was isolated (11,363 g, 20 min) immediately for fluorescence detection ($\lambda_{em}/\lambda_{ex}$: 326/432 nm) on a multiplate reader (Synergy H1, Biotek, USA). The mixture of H_2O_2 (10 μM) and Fe^{2+} (30 μM) and ultrapure water were used as positive control and negative control, respectively. The results were expressed as relative fluorescent intensity compared to negative control.

2.6. X-ray photoelectron spectroscopy (XPS) analysis

ZIF-8 and ZIF-67 (3.7 nM) were incubated with 2×10^6/mL Rb for 10 min and washed with PBS for three times. The as-prepared samples were lyophilized to get powder for XPS analysis (AXIS Supra, Kratos Analytical Inc.). All spectra were calibrated by the peak of C 1 s (284.8 eV).

2.7. Quantitative analysis for cellular adsorption and internalization of ZIF-67

Rb (2×10^6/mL) was incubated with ZIF-67 (3.7, 7.5, and 15 nM in PBS) for 10 min. The mixture was then lysed with RIPA after PBS washing (three times). One aliquot was collected to detect the total content of ZIF-67 adsorbed and internalized by Rb. Another aliquot was centrifuged at 2000 g to remove cell membrane and the supernatant was further centrifuged at 11,363 g to pellet the ZIF-67 internalized by Rb. The two kinds of samples were digested with H_2O_2:HNO_3 (v:v, 2:1) for 12 h and analyzed for Co on a NexION 350D inductively coupled plasma mass spectrometry (ICP-MS).

2.8. Quantitation of intracellular protein adsorbed by ZIF-67

Rb (2×10^6/mL) was incubated with ZIF-67 (0.9, 1.8, 3.7, 7.5, and 15 nM in PBS) for 10 min. After washing with PBS for three times, the sample was lysed with RIPA and centrifuged (2000 g) to remove cell membrane. Then, the bioconjugate of ZIF-67 and protein was isolated from supernatant by centrifugation at 11,363 g for 20 min. The as-prepared sample was washed with PBS and followed by BCA assay for protein quantitation.

2.9. Characterization of the bioconjugates of hemoglobin and ZIF-67

Hemoglobin (1 μM) was incubated with ZIF-67 (3.7 nM) for 10 min and the bioconjugate was dropped onto a copper grid for 15 min. The as-prepared sample was dried overnight for transmission electron microscopy (TEM, JEM-2100, JEOL, Japan) observation. The hydrodynamic sizes of bioconjugates of hemoglobin and ZIF-67 were measured on a Malvern Nano ZS. The efficiency of protein adsorption was evaluated by BCA method. Different concentrations of ZIF-67 (0.9, 1.8, 3.7, 7.5, and 15 nM in PBS) were mixed with hemoglobin (1 μM) at room temperature for 10 min. After 11,363 g centrifugation, the supernatant was isolated for protein concentration measurement. The efficiency (A%) was calculated by following equation: $A\% = 1 - C/C_0$. Where C and C_0 are the concentrations of hemoglobin with or without ZIF-67, respectively.

2.10. Spectroscopic analysis for the structural change of hemoglobin

Hemoglobin (1 μM) was mixed with ZIF-67 (0.07, 0.15, 0.37, and 0.75 nM in PBS) for 10 min and the fluorescence spectra were recorded on an F-4600 fluorescence spectrophotometer (Hitachi, Japan). The excitation wavelength was set at 278 nm and fluorescence emission intensities at 344 nm against the molar concentration of ZIF-67 were fitted to Stern-Volmer equation after correction of inner filter effect (Kubista et al., 1994).

Ultraviolet visible (UV–vis) spectra were measured by incubating 1 μM hemoglobin with ZIF-67 for 10 min. The absorbance of sample was recorded on a UV-3600 spectrophotometer (Shimadzu, Japan) from 250 to 550 nm.

Circular dichroism (CD) spectra were obtained on a Chirascan V100 spectropolarimeter (Applied photophysics, UK) with 0.1 cm quartz cell. The hemoglobin (2 μM) was treated with ZIF-67 (0.07, 0.15, 0.37, and 0.75 nM in PBS) for 10 min and the sample was measured from 205 nm to 300 nm.

2.11. Heme release detection

Hemoglobin (0.8 mM) was incubated with ZIF-67 (1.8, 3.7, and 7.5 nM in PBS) or urea (2.5 M, positive control) for 10 min. After the addition of 0.1 M ammonium acetate (pH 4.0), the samples were washed with the mixture of methanol:chloroform (5 mL; v:v, 1:2). The organic phase was vapored and residues were redissolved into DMSO:chloroform (0.5 mL; v:v, 1:4) followed by the addition of NaOH (1 mL, 0.1 M) (Rael et al., 2006). The percentage of heme release was calculated from following equation: $A\% = (A_1\text{-}A_b)/A_p$. Where A_1, A_b, and A_p represent the absorbance (385 nm) of sample, background, and positive control, respectively.

2.12. Molecular dynamic (MD) simulation of heme release

The structure of hemoglobin and ZIF-67 were obtained from the Protein Data Bank (www.rcsb.org; PDB ID: 4MQJ) and the Cambridge Crystallographic Data Centre (www.ccdc.cam.ac.uk), respectively. All-atom MD simulation was performed using GROMACS software (version 2016.3) coupled with CHARMM-GUI webserver. CHARMM36m all-atom force field parameters for protein, water molecule, and ions (Na^+, Cl^-) were used and bonded and non-bonded parameters compatible to CHARMM36m force field for ZIF-67 were constructed to set up all the simulation systems during MD simulation (Huang et al., 2017). System snapshots were generated by VMD.

2.13. Statistical analysis

All data were presented as mean ± standard deviation with at least three dependent assays. The *t*-test was used for significance analysis. The significant differences were set as * $p < 0.05$ and * * $p < 0.01$.

3. Results and discussion

3.1. Hemolysis assessment of ZIF-8 and ZIF-67

ZIF-8 and ZIF-67 were prepared according to Feng et al (Feng et al., 2016). The as-prepared ZIF-8 and ZIF-67 were characterized by TEM, powder X-ray diffraction (PXRD) spectrometry, and dynamic light scattering (DLS). ZIF-8 and ZIF-67 show spherical morphology with similar solid sizes (33.53 ± 0.54 and 35.72 ± 0.21 nm, respectively) (Fig. 1A and Fig. S1), hydrodynamic diameters (106.2 ± 4.7 and 112.7 ± 8.9 nm, respectively) (Fig. 1B), PXRD patterns (Fig. 1C), pore sizes, (Fig. S2) and porosities (Table S1). ZIF-8 and ZIF-67 gave positive zeta potentials of 31.27 ± 1.24 mV and 22.85 ± 1.67 mV, respectively (Fig. 1D), and were stable in PBS (Fig. S3). However, the ZIFs dissolved in blood with maximum percentage of 1.82% and 5.22% for ZIF-8 and ZIF-67 (Fig. S4), respectively, which may be induced by the ions and phosphates in blood with strong coordination ability after 24 h incubation.

We firstly investigated the effect of ZIF-8 and ZIF-67 on the morphology of Rb as the function of Rb relies on its normal shape. Rb is a sensitive model for the assessment of the hematotoxicity of NPs. Hemolysis is related to various kinds of diseases (Rother et al., 2005), so NPs induced hemolysis is harmful to human health. Thus, hemolysis is considered as the key indicator in hematotoxicity (de la Harpe et al., 2019). LSCM images show that the morphology of Rb was intact in negative control group (PBS) (Fig. 1E(i)) but destroyed in positive control group (ultrapure water) (Fig. 1E(ii)). ZIF-8 at both low (0.9 nM) and high (7.5 nM) concentrations had no significant effect on the shape of Rb (Fig. 1E (iii, iv)). Also, ZIF-67 at low concentration (0.9 nM) did not change the shape of Rb significantly (Fig. 1E(v)). However, ZIF-67 at high concentration (7.5 nM) did lead to significant transformation of the shape of Rb (Fig. 1E(vi)). Thus, ZIF-67 was prone to influence the morphology of Rb at high concentration.

Shape transformation and membrane deformation of Rb are usually associated with hemolysis, and thought as the key indicator in hematotoxicity (Barbul et al., 2018). Therefore, scanning electron microscopy (SEM) images were collected to show the change in the membrane morphology of Rb and the distribution of the ZMOFs. Several large aggregates of ZIF-67 (ca. 0.93 μm) were attached onto the distorted membrane of Rb (Fig. S5 and S6). ZIF-67 induced different sizes of pores (0.01–1.06 μm) on the membrane of Rb which trapped the aggregated ZIF-67. In contrast, ZIF-8 showed small aggregates (ca. 0.53 μm) and did not induce such membrane destruction (Fig. S5 and S6). These results

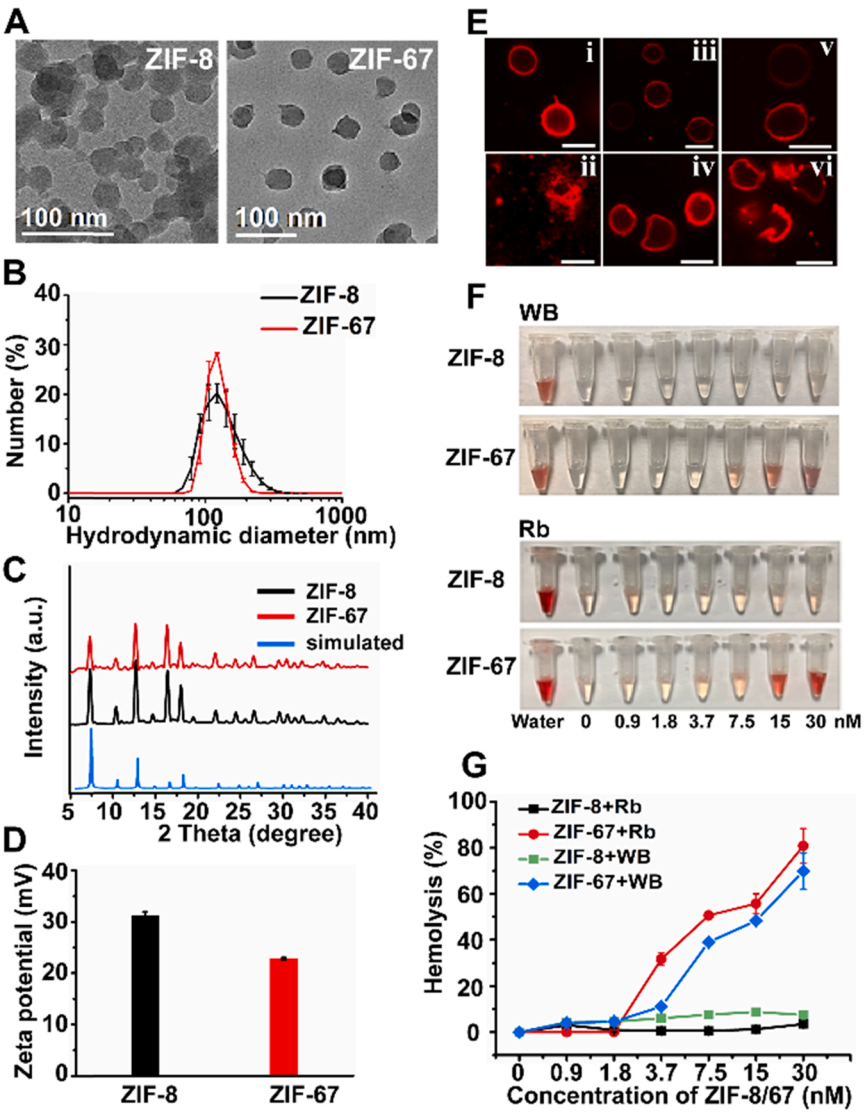

Fig. 1. (A) TEM images of the as-prepared ZIF-8 and ZIF-67. (B) Hydrodynamic diameters of the as-prepared ZIF-8 and ZIF-67 in ultrapure water. (C) PXRD patterns of the as-prepared ZIF-8, ZIF-67, and simulation. The diffraction peaks were in good agreement with the simulated curve, indicating the products are pure-phase materials. (D) Zeta potentials of the prepared ZIF-8 and ZIF-67 in ultrapure water. (E) LSCM images of Rb after incubation with various solutions: (i) PBS (negative control), (ii) ultrapure water (positive control), (iii) 0.9 nM ZIF-8, (iv) 7.5 nM ZIF-8, (v) 0.9 nM ZIF-67, and (vi) 7.5 nM ZIF-67. Scale bars, 5 μm. (F) Photographs of the supernatant of Rb after incubation with ZIF-8 and ZIF-67. Test groups (from left to right): ultrapure water, 0 nM, 0.9 nM, 1.8 nM, 3.7 nM, 7.5 nM, 15 nM, and 30 nM ZIF-8 or ZIF-67, respectively. (G) Hemolysis curves of WB and Rb incubated with ZIF-8/67 at room temperature for 10 min.

indicate only ZIF-67 induced the structural change of Rb membrane.

ZMOFs induced hemolysis was also explored in the solution of WB and Rb. Visible detection of the solution color and UV–vis spectrometric determination were used to confirm the hemoglobin released due to hemolysis (Fig. 1F and G). The concentration of the released hemoglobin in the supernatant of WB significantly increased with the concentration of ZIF-67 from 0.9 to 30 nM, while ZIF-8 in the same concentration range did not induce obvious release of hemoglobin. Similarly, only ZIF-67 induced hemoglobin release in Rb solution. The hemolysis percentages were plotted against the concentrations of ZMOFs. ZIF-67 caused bigger hemolysis percentage (from 0.0 ± 0.0% to 80.8 ± 7.5%) in Rb solution than in WB solution (from 0.0 ± 0.0% to 69.8 ± 7.9%), which suggests the plasma protein decreased the hemolysis. The ZIFs could adsorb the negatively charged plasma protein (such as albumin) and the formation of corona significantly changed the surface properties of ZIFs. The zeta potentials of ZIFs changed to about −20 mV after adsorption of serum (Fig. S7) and partially inhibited the interaction between ZIFs and Rb, reducing the hemolysis ratios in WB solution (Fig. 1G). In contrast, ZIF-8 had no hemolysis effect in either Rb or WB solution. Time-dependent hemolysis assay also shows the hemolysis percentage of Rb induced by ZIF-67 reached 37.1% in 10 min and then slowly increased with further increase of time (Fig. S8).

Considering the possible release of the metal ion from ZIF-8 and ZIF-67 may induce hemolysis, the stability of ZIF-8 and ZIF-67 after incubation with Rb was tested by ICP-MS and PXRD spectrometry. Both ZIF-8 and ZIF-67 were stable in Rb solution as only 0.0%–0.9% and 0.0%–2.6% of ZIF-8 and ZIF-67 dissolved in Rb solution within 10 min, respectively (Fig. S9) and the diffraction peaks did not change (Fig. S10). According to the dissolved metal ion concentrations (10–172 μg/mL for Zn(II) and 26–516 μg/mL for Co(II)), the hemolysis assay was performed with Co(II) and Zn(II) (Fig. S11). The result shows that hemolysis did not result from the dissolved metal ions from the ZMOFs. As hemolysis assessment shows that ZIF-67 was hematoxic while ZIF-8 was hemocompatible in the same concentration range, the metal ions in the ZMOFs played important roles in the toxicology of the ZMOFs.

3.2. Hemolysis mechanism

Clarifying the mechanism for the big difference in the hemolysis of ZIF-8 and ZIF-67 is important for the biosafety assessment of ZMOFs. Phospholipid is the most abundant constituent of cell membrane and its conformational change is usually associated with membrane breakage (de la Harpe et al., 2019; Wang and Jiang, 2015). Therefore, Fourier transform infrared (FTIR) spectrometry fitted with an attenuated total reflectance (ATR) accessory was used to reveal the structural change of phospholipid in situ. For this purpose, the FTIR spectra of Rb before and

after incubation with ZIF-8 and ZIF-67 were obtained in the fingerprint region of 800–1400 cm^{-1} (Fig. 2A) to compare the FTIR spectra of ZIF-8 and ZIF67 (Fig. S12). The characteristic band of 1367 cm^{-1} (the vibration of methylene fragments of lipid) (Wang and Jiang, 2015) disappeared after incubation with ZIF-67, whereas this band still remained after incubation with ZIF-8. The bands in the range of 1240–1244 cm^{-1} (asymmetric stretching vibration of PO_2^-) (Wrobel et al., 2011) disappeared after incubation with ZIF-67, indicating significant change of the lipid structure. The band at 1167 cm^{-1} for the stretching mode of cholesteryl esters (-CO-O-C-) (Parikh and Chorover, 2006) disappeared after incubation with ZIF-8 and ZIF-67, suggesting that ZIF-8 and ZIF-67 impacted the structure of cholesterol. The new band of 1013 cm^{-1} after incubation with ZIF-8 and ZIF-67 stand for the coordination of oxygen atom of phospholipid with Zn or Co atom (Ansari et al., 2014). The above FTIR results confirm that ZIF-67 made stronger effect on the conformation of phospholipid than ZIF-8.

The generation of ROS by the ZMOFs was evaluated to demonstrate the contribution of ROS to the breakage of Rb membrane. It was reported that the ROS generated by NPs was responsible for phospholipid and membrane destruction (Bai et al., 2020). In this work, we used DCFH-DA as the turn-on fluorescence probe for ROS detection (Aranda et al., 2013). We found that ZIF-67 produced ROS in a dose-dependent manner, while ZIF-8 had much lower ability for ROS generation in the same concentration range (Fig. 2B). Furthermore, the deletion of ROS by glutathione (GSH) significantly reduced the hemolysis percentage in ZIF-67 treated group (Fig. 2C *c.f.* Fig. 1G). The result suggests that the ROS produced by ZIF-67 was responsible for the destruction of the lipid structure and Rb membrane.

The species of ROS was further explored to illustrate the mechanism of ROS generation. The generation of superoxide anions ($O_2^{\bullet-}$) was firstly evaluated by a classic NBT chromogenic assay. The result shows the absorbance of NBT at 650 nm increased with the concentration of ZIF-67, suggesting the increasing generation of $O_2^{\bullet-}$ (Fig. 2D). The generation of hydroxyl radical (•OH) was revealed with TPA as a fluorescent probe. The fluorescent intensity of TPA increased with concentration of ZIF-67, indicating the increasing production of •OH (Fig. 2E). ZIF-67 has superoxide dismutase (SOD)- and catalase-like activities to catalyze $O_2^{\bullet-}$ to H_2O_2 and H_2O_2 to •OH, respectively (Sang et al., 2020). Therefore, we proposed the possible mechanism for ZIF-67 induced ROS generation as illustrated in Fig. 2F. The Co(II) of ZIF-67 reacted with O_2 to form $O_2^{\bullet-}$, then catalyzed $O_2^{\bullet-}$ to form H_2O_2, and further degraded H_2O_2 to generate •OH with the transformation of chemical state from Co (II) to Co(III). XPS was used to confirm the change in the chemical state of Co in ZIF-67 after incubation with Rb. ZIF-67 gave the characteristic peaks of Co^{2+} at 781.4 and 796.8 eV before incubation with Rb, but produced new peaks for Co^{3+} appeared at 780.4 and 798.6 eV after incubation with Rb (Fig. 2G), supporting the mechanism for ROS generation.

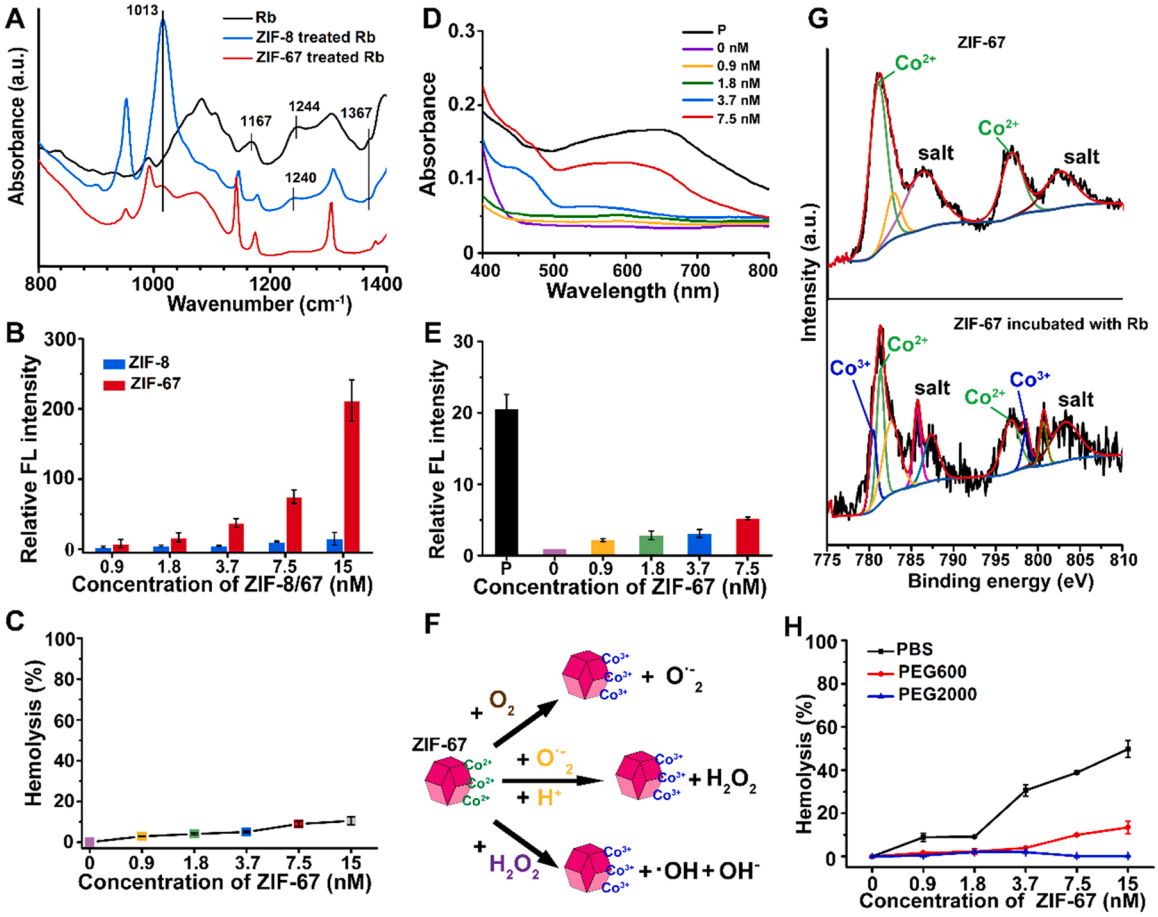

Fig. 2. (A) FTIR spectra for Rb, ZIF-8 treated Rb, and ZIF-67 treated Rb. Concentration of ZIF-8 and ZIF-67, 3.7 nM. (B) Relative fluorescence (FL) intensity of DCFH-DA due to the ROS generated by ZIF-8 and ZIF-67 compared to negative control (PBS, 6.7 mM, pH 7.4). (C) Hemolysis percentage of Rb incubated with ZIF-67 in the presence of GSH (100 μM). (D) UV–vis absorption spectra of NBT in various concentrations of ZIF-67 solution. The mixture of riboflavin (20 μM) and methionine (13 mM) was used as positive control (P). (E) Relative FL intensity of TPA due to the •OH generated by ZIF-67 compared to negative control (PBS, 6.7 mM, pH 7.4). The mixture of Fe^{2+} (30 μM) and H_2O_2 (10 μM) was used as positive control (P). (F) Mechanism for the generation of $O_2^{\bullet-}$ and •OH induced by ZIF-67. (G) High resolution XPS spectra of ZIF-67 before (top) and after (bottom) incubation with Rb. (H) Osmoprotection assay of the hemolysis induced by ZIF-67. Concentration of PEG600 and PEG2000, 30 mM.

Though ROS induces the membrane destruction and hemolysis, the mechanism of hemolysis is still not fully understood. Previous studies show that the mechanism of hemolysis includes the formation of nano-sized lesions induced by osmolarity dysfunction, influx of small ions, and swelling and rupture of membrane with formation of large pores (Sovadinova et al., 2011; Kettiger et al., 2016). We assume that the ROS generated by ZIF-67 disturbs the phospholipid structure and brings up the osmolarity dysfunction, leading to the formation of membrane lesions. To this point, the osmoprotection assay was carried out as the solute molecule in osmoprotection solution could fill up the membrane lesion to reduce the hemolysis (Sovadinova et al., 2011). Fig. 2H shows that PEG600 significantly reduced the percentage of hemolysis while PEG2000 completely inhibited hemolysis, suggesting the hypothesis was correct. In general, the mechanism of hemolysis can be described as follows: the ROS produced by ZIF-67 changes the structure of phospholipid, then the regulative function of membrane is lost, which brings up the formation of small lesions; finally, ions flow into Rb and induce large pores.

Considering ZIF-8 did not induce membrane deformation and structure change of phospholipid while ZIF-67 was hematotoxic, we then used ZIF-67 to further investigate the hematotoxic effects in following experiments.

3.3. Cellular internalization of ZIF-67 and characterization of bound protein

It is significant to study the behavior of ZIF-67 inside Rb after cellular internalization for further understanding its hematotoxicity. TEM image shows that lots of ZIF-67 was adsorbed on Rb and small clusters of ZIF-67 were surrounded by Rb (Fig. 3A). Rb showed no nucleus and most organelles to accommodate maximum space for hemoglobin (Daugas et al., 2001). Besides, ZIF-67 was internalized by Rb (yellow square) and the magnification image confirms that the shape of internalized ZIF-67 was similar to that of pristine ZIF-67 (Fig. 3A*c.f.* Fig. 1A).

The content of ZIF-67 adsorbed and/or internalized by Rb was then measured by ICP-MS (Fig. 3B). The total content of ZIF-67 adsorbed and internalized by Rb ranged from 13.21 ± 0.12–57.25 ± 0.69 μg/10^6 cells (as Co) as the initial concentration of ZIF-67 increased from 3.7 to 15 nM (Fig. 3C). However, the content of internalized ZIF-67 by Rb increased from 2.28 ± 0.09–2.63 ± 0.03 μg/10^6 cells, then decreased to 1.68 ± 0.01 μg/10^6 cells (as Co) as the initial concentration of ZIF-67 increased (Fig. 3D) because the aggregated ZIF-67 was too large to be internalized by Rb, which reduced the intracellular content of ZIF-67. Similar result was also found for silica NPs: large sized silica NPs had lower cellular uptake efficiency than small ones (Chen et al., 2019).

The proteins inside Rb could be adsorbed by the internalized ZIF-67. The content of adsorbed proteins was measured by the BCA assay. The content of adsorbed proteins increased from 1.07 ± 0.02–1.29 ± 0.11 μg and then decreased to 0.86 ± 0.02 μg as the initial concentration of ZIF-67 increased (Fig. 3E), in good agreement with the pattern for the change of the internalized ZIF-67 with initial concentration of ZIF-67 (Fig. 3D). As the hemoglobin accounts for 90% of total proteins in Rb, the proteins adsorbed by NPs after cellular internalization is mainly hemoglobin (Zhao et al., 2017). Western blot experiment confirms that the bands of subunit of hemoglobin appeared at 15 kDa after incubation of Rb and ZIF-67 (Fig. 3F). The pattern for the adsorbed hemoglobin was similar to that for the internalized ZIF-67 (Fig. 3F *c.f.* Fig. 3D). The above results demonstrate that ZIF-67 was internalized by Rb and the internalized ZIF-67 adsorbed intracellular hemoglobin, which may lead to the alteration of protein conformation and function.

3.4. Adsorption of hemoglobin on ZIF-67

Study on the adsorption of hemoglobin on ZIF-67 can help to understand the conformational change of hemoglobin and to evaluate the hematotoxicity at molecular level. The adsorption characteristics of hemoglobin on ZIF-67 was further explored in a standard solution. TEM was used to observe the morphology of the bioconjugate of ZIF-67 and hemoglobin. Fig. 4A shows that the ZIF-67 (white arrow) was surrounded by hemoglobin. ZIF-67 was stable in hemoglobin solution because the extent of dissolved ZIF-67 was very low (0.01–1.50%) (Fig. S13) and the PXRD pattern of ZIF-67 kept steady (Fig. S14).

The bioconjugate of ZIF-67 and hemoglobin was characterized by DLS. The hydrodynamic diameters of the bioconjugate increased from 96.39 ± 18.66 nm to 865.31 ± 19.01 nm with the concentration of hemoglobin from 0.6 to 20 μM (Fig. 4B), suggesting the formation of aggregates. Previous studies also found that proteins could induce aggregation of NPs (Dominguez-Medina et al., 2016; Bharti et al., 2011). For instance, low concentration of BSA induced the aggregation of gold

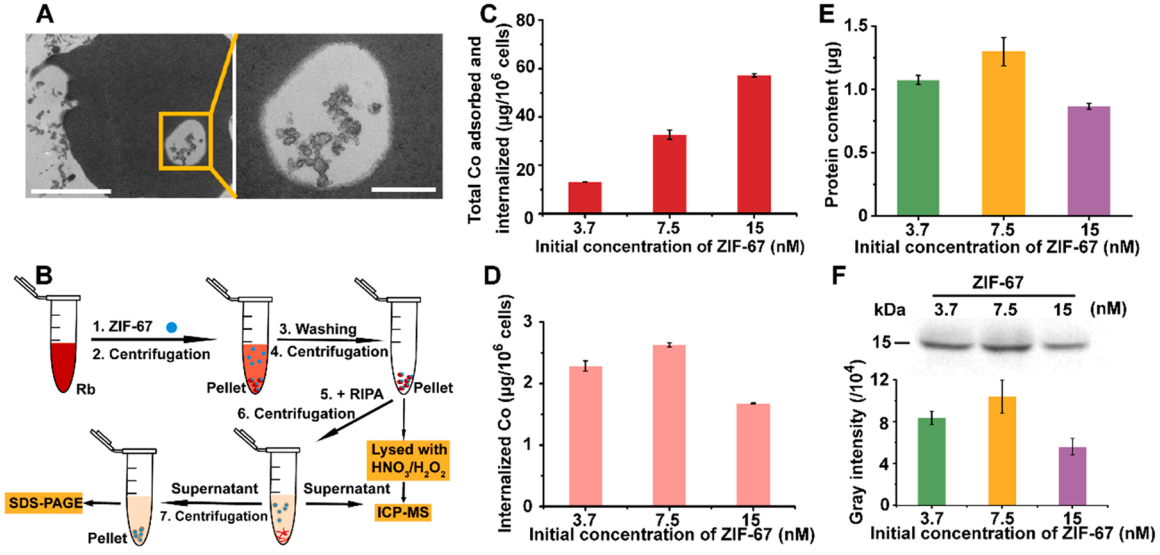

Fig. 3. (A) TEM images of cellular internalization of ZIF-67. Scale bars, 2 μm (left) and 500 nm (right). (B) Scheme for the experimental procedure of cellular behavior of ZIF-67. (C) Total content of the ZIF-67 adsorbed and internalized by Rb (as Co) against the initial concentration of ZIF-67. (D) Content of ZIF-67 internalized by Rb (as Co) against the primary concentration of ZIF-67. (E) Concentration of total protein adsorbed by intracellular ZIF-67. (F) Western blot analysis to identify the hemoglobin adsorbed by intracellular ZIF-67 (top), and gray intensity of hemoglobin band in ZIF-67 group (bottom).

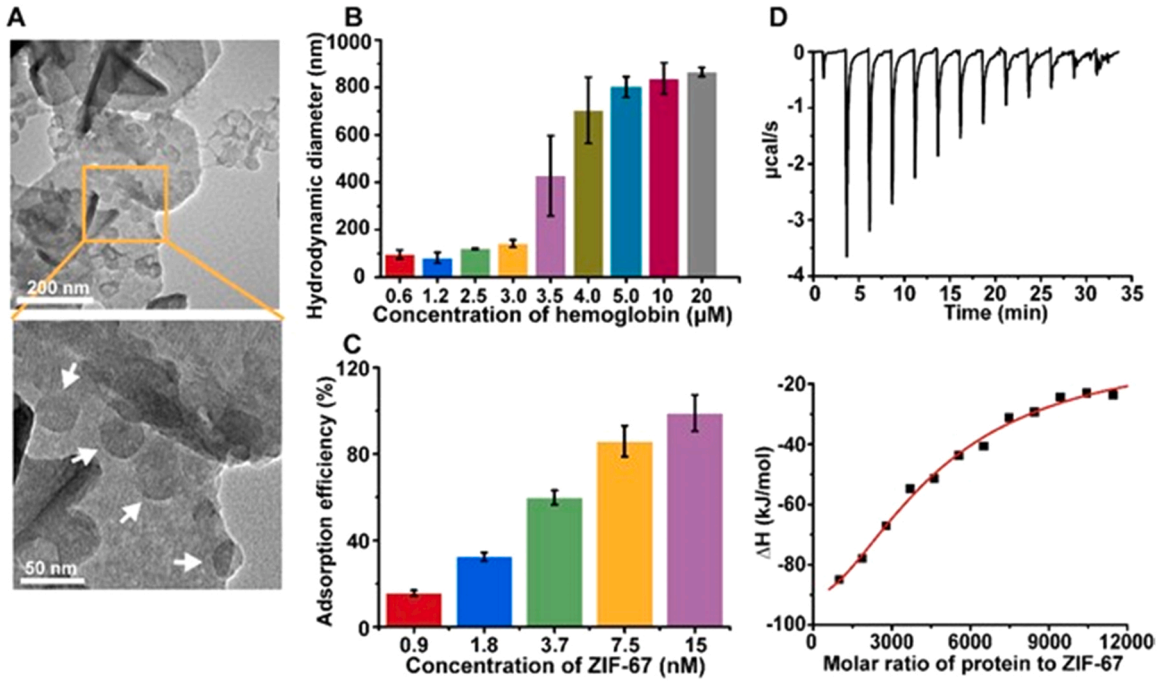

Fig. 4. (A) TEM images of the bioconjugates of hemoglobin and ZIF-67. Concentrations of hemoglobin and ZIF 67 were 1.0 μM and 7.5 nM, respectively. (B) Hydrodynamic sizes of the bioconjugates of ZIF-67 (7.5 nM) and hemoglobin. (C) Adsorption efficiency of hemoglobin (1.0 μM) incubated with different concentrations of ZIF-67. (D) ITC titration plot (top panel) and fitted curve (bottom panel) for the binding of ZIF-67 to hemoglobin at 298 K.

nanorod by unfolding protein (Dominguez-Medina et al., 2016). Silica NPs aggregated after the addition of lysozyme at specific pH condition (Bharti et al., 2011). However, further increase of the hydrodynamic size of aggregates is limited due to the "dynamic adsorption equilibrium" (Zhao et al., 2017). Thus, the hydrated particle size of the bioconjugates became stable at ~860 nm when the hemoglobin concentration reached to 10 μM.

The adsorption efficiency was evaluated by the BCA assay to obtain the adsorption capacity for the ZIF-67 under the aggregation condition. The adsorption efficiency increased from 15.6% to 98.9% with the concentration of ZIF-67 from 0.9 to 15 nM (Fig. 4C). However, the number of protein molecules adsorbed per ZIF-67 nanoparticle decreased significantly from 26.0 to 3.3 in the same concentration range due to the aggregation-induced reduction in the surface area of ZIF-67 (Fig. S15).

The adsorption of protein to NPs could be driven by a variety of binding forces, such as hydrogen bonding, electrostatic interaction, and van der Waal force. Elucidating the thermodynamic parameters would help to understand the binding forces and thermodynamic process. To this end, isothermal titration calorimetry (ITC) was used to obtain the enthalpy change (ΔH) and binding affinity constant (K_d) for the adsorption of hemoglobin to ZIF-67. The changes of entropy (ΔS) and the Gibbs free energy (ΔG) were then calculated according to $\Delta G = \Delta H - T\Delta S = -RT\ln K_d$ (Hu et al., 2009). The adsorption of hemoglobin to ZIF-67 was an exothermic process with the heat change from −3.7 to −0.5 μcal/s (Fig. 4D). The values of ΔH and K_d were −335 kJ/mol and 1.5 μM, respectively, while those of ΔG and ΔS were −33.2 kJ/mol and −1.0 kJ/mol, respectively (Table S2).

The parameters ΔH and ΔS are associated with the types of binding forces. According to the Ross' theory (Ross and Subramanian, 1981), the occurrence of $\Delta H < 0$ and $\Delta S < 0$ indicates that the hydrogen bonding and van der Waal force dominate the adsorption with the structural change of protein. Besides, the stoichiometry (n) of the interaction was 11.9, showing that about twelve protein molecules were adsorbed per ZIF-67 nanoparticle.

3.5. ZIF-67 induced conformational change of hemoglobin

NPs could change the structure of proteins and induce severe diseases (Cai and Chen, 2018). The effect of ZIF-67 on the structure of hemoglobin was studied by fluorescence, UV–vis, and CD spectrometry to illustrate the toxicological effect of ZIF-67 at molecular level. Prior to spectroscopic evaluation, the stability of the bioconjugate of ZIF-67 and hemoglobin was measured. The result in Table S3 shows the hydrodynamic diameters of the bioconjugates of ZIF-67 and hemoglobin had no significant change with time, which excluded the effect of precipitation or aggregation of particles on spectral intensities. The fluorescence of hemoglobin decreased as the concentration of ZIF-67 increased from 0.07 to 0.75 nM, indicating the change of the microenvironment of the aromatic fluorophores (tryptophan, tyrosine, and phenylalanine) from hydrophobicity to hydrophilicity (Fig. 5A) as the access of water molecule to fluorophores decreased the fluorescence emission (Yang et al., 2013; Hao et al., 2015; Zhao et al., 2015b). The Stern-Volmer plot for ZIF-67 induced fluorescence quenching of hemoglobin is shown in Fig. S16. The obtained quenching constant (k_q) of 6.8×10^{16} /M/s (Table S4) is higher than the maximum diffusion collision quenching constant, indicating a static quenching mechanism due to the formation of the ground-state complex with ZIF-67 (Zhao et al., 2015a).

The UV–vis absorption spectra gave information on the structural change of hemoglobin. Fig. 5B shows hemoglobin had characteristic peaks at 275 nm (fluorophore band) and 405 nm (Soret band). The fluorophore band decreased a lot and exhibited a red shift from 275 nm to 280 nm as the concentration of ZIF-67 increased from 0.07 to 1.5 nM. This result indicates the microenvironment of fluorophore changed from hydrophobicity to hydrophilicity, which in good agreement with the result from fluorescence spectra in Fig. 5A. The Soret band was induced by the π→π * electronic transition of porphyrin ring (heme) in hemoglobin and its decrease represented the structural transformation of hemoglobin (Shao et al., 2011), suggesting the exposure of the heme to the aqueous medium (Mahato et al., 2010). The hypochromicity in fluorescence and UV–vis spectra indicates the fluorophore and heme of hemoglobin experienced conformational alteration in binding with

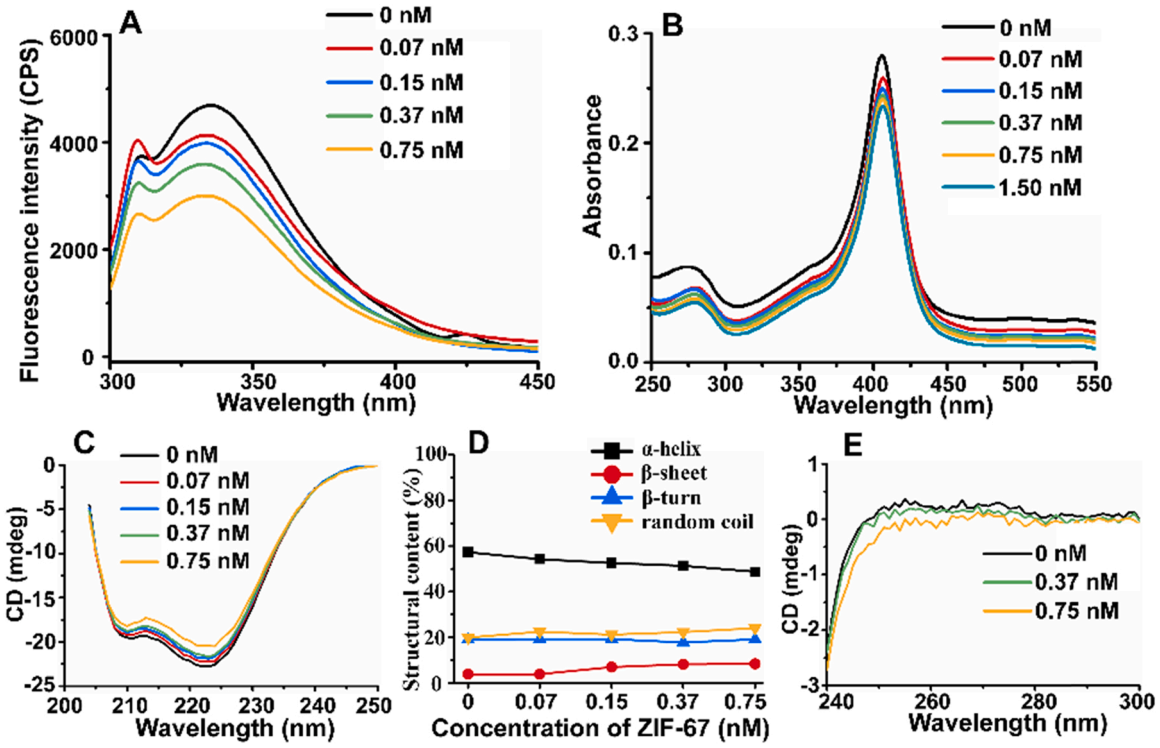

Fig. 5. Fluorescence spectra (A), UV–vis spectra (B), and CD spectra (C) of hemoglobin incubated with different concentrations of ZIF-67. (D) Change of secondary structure of hemoglobin with ZIF-67 concentration calculated from the CD spectra in (C). (E) Near-UV CD spectra of hemoglobin after incubation with ZIF-67. Concentration of hemoglobin was fixed at 1 μM in all groups and incubation time was 10 min.

ZIF-67.

The effect of ZIF-67 on the secondary structure of hemoglobin was studied by CD spectrometry due to its important role in hemoglobin function. The far-UV CD spectra of hemoglobin show two characteristic peaks of α-helix at 208 and 222 nm (Fig. 5C) (Zhao et al., 2017). The intensity of the α-helix peaks increased with the concentration of ZIF-67, suggesting the change of the secondary structure of hemoglobin upon binding with ZIF-67. Fig. 5D shows the change of the contents of α-helix, β-sheet, random coil and β-turn with the concentration of ZIF-67. The content of α-helix decreased from 57.3% to 47.6% as the concentration of ZIF-67 increased from 0 to 0.75 nM. Meanwhile, the contents of β-sheet and random coil increased from 3.80% to 8.42% and 19.9–24.1%, respectively, but the content of β-turn did not change significantly. These results suggest that ZIF-67 altered the secondary structure of hemoglobin with unfolding of protein. The near-UV spectra from 240 to 300 nm present useful information on the tertiary structure of hemoglobin (Fig. 5E). The decreased CD intensity indicates that the tertiary structure of hemoglobin was destroyed as the concentration of ZIF-67 increased.

3.6. Functional assessment of hemoglobin upon binding with ZIF-67

Conformational change could affect the function of hemoglobin, leading to toxicity at molecular level. The effect of ZIF-67 on the capacity of oxygen binding and releasing was evaluated. The saturation percentage of hemoglobin was determined by measuring the absorbance at 505 (oxyhemoglobin) and 575 nm (deoxyhemoglobin) relative to negative control (without ZIF-67). As the concentration of ZIF-67 increased from 0 to 7.5 nM, the percentage of saturation in oxygen carrying decreased from 100.0% to 6.4 ± 2.7% (Fig. 6A), while the percentage of saturation in oxygen releasing increased from 0.0% to 33.9 ± 5.9% (Fig. S17). These results indicate that ZIF-67 significantly reduced the capacity of oxygen binding and impeded the oxygen release from hemoglobin.

The heme release from hemoglobin at the positions of His-α58 and His-β63 could inhibit the oxygen binding and releasing (Olson et al., 1997), leading to the dysfunction of hemoglobin. To address this issue, spectroscopic measurement was performed to obtain the relative content of heme releasing from hemoglobin after incubation with ZIF-67 (Fig. 6B). The percentage of the released heme raised from 21.4 ± 0.4% to 38.2 ± 7.7% with the increase of the concentration of ZIF-67 from 1.8 to 7.5 nM. We then used MD simulation to understand the mechanism of heme release from hemoglobin. Fig. 6C shows the snapshot of the interaction of ZIF-67 and hemoglobin at the end of simulation. The ZIF-67 was close to the heme group upon the hydrophilic surface of hemoglobin (Fig. S18) and the distance between the hydrogen and oxygen atom of heme was close enough to interact with the nitrogen and the cobalt atoms of ZIF-67, which may drive the release of heme. As previous studies confirmed that the salt bridge (including hydrogen bond and electrostatic interaction) governs the interaction of protein and nanoparticles (Cao et al., 2021; Wang et al., 2018), the number of hydrogen bonds was firstly evaluated. Results in Fig. 6D indicate that the average number of hydrogen bonds (0.08) for ZIF-67 and heme was lower than that (2.39) for hemoglobin and heme, which means the release of heme was not induced by hydrogen bonds. However, the average energy of electrostatic interaction in the group of ZIF-67 and heme (−269.87 kJ/mol) was significantly higher than that in the group of hemoglobin and heme (5.14 kJ/mol) (Fig. 6E), confirming that the electrostatic interaction was the main force for the release of heme. The effect of ionic strength on the binding of heme to ZIF-67 was performed to verify the MD result as the improvement of ionic strength would mask the electrostatic interaction and inhibit the heme release. Fig. S19 shows the percentage of heme adsorption decreased as ionic strength increased from 124 to 310 mM, confirming that the electrostatic interaction induced heme release.

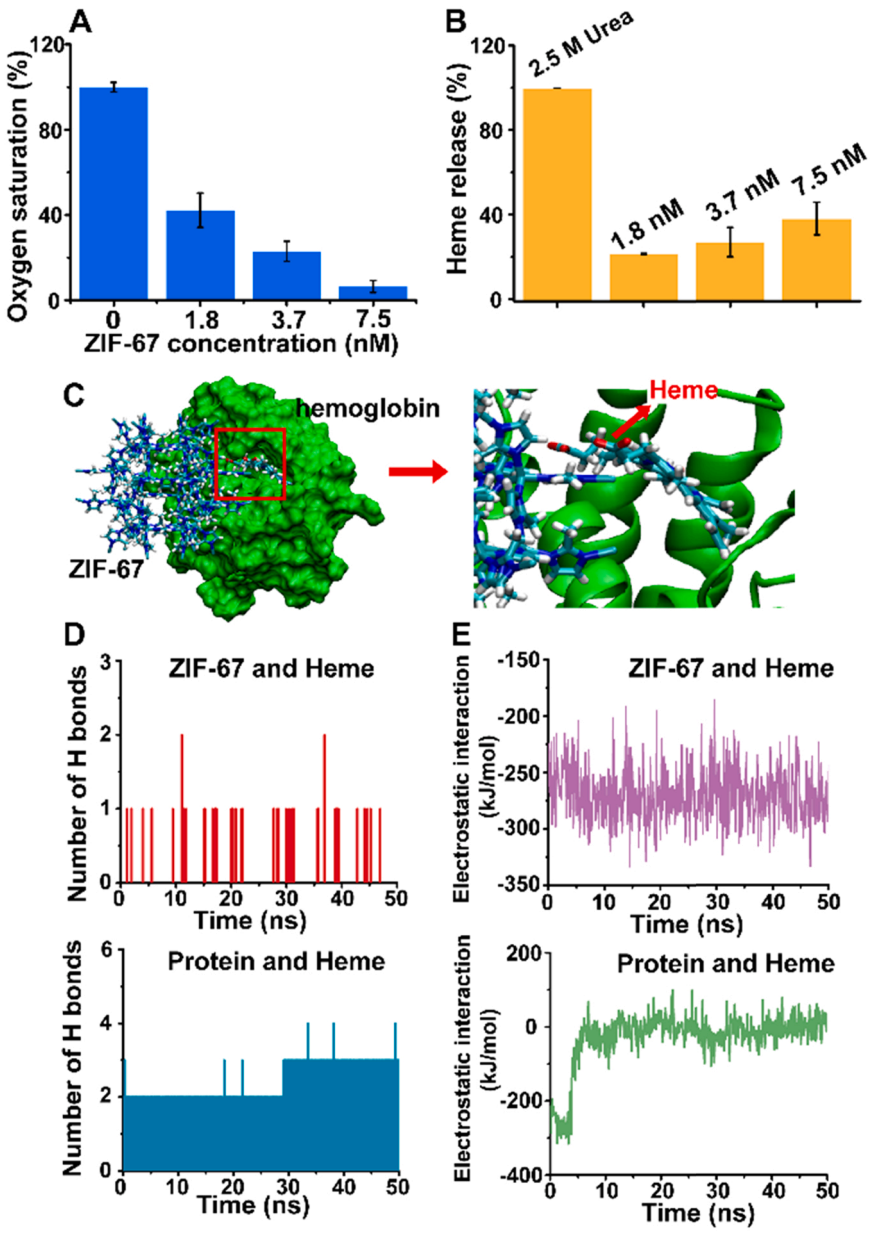

Fig. 6. (A) Capacity of oxygen carrying for hemoglobin exposed to different concentrations of ZIF-67. (B) Percentage of heme release with the treatment of ZIF-67 relative to positive control (2.5 M urea). (C) Snapshot for the interaction of ZIF-67 and the subunit of hemoglobin. Red square represents magnification area. (D) Number of hydrogen bonds. (E) Energy of electrostatic interaction.

4. Conclusion

We have reported the hematotoxicity of two typical nano-sized MOFs ZIF-8 and ZIF-67. ZIF-67 gave significant hemolysis for Rb due to the ROS-induced osmolarity dysfunction of membrane whereas the ZIF-8 was hematocompatible. ZIF-67 bound with hemoglobin via hydrogen bond and van der Waals force after internalization by Rb. The microenvironments and secondary structure of hemoglobin changed significantly upon binding to ZIF-67. The interaction with ZIF-67 dramatically inhibited the function of hemoglobin in oxygen carrying and releasing in accompany with heme release from hemoglobin due to electrostatic interaction between heme and ZIF-67. The findings herein reveal the blood biocompatibility of the two important MOFs and the mechanism of their hematotoxicity at molecular level, providing the risk assessment of MOFs from biomedical and toxicological aspects.

CRediT authorship contribution statement

Hao Fang: Conceptualization, Methodology, Writing – original draft. **Yan Xiu-Ping:** Supervision, Project administration, Writing – review & editing, Funding acquisition.

Declaration of Competing Interest

The authors declare no competing financial interest.

Acknowledgements

This work was supported by the National Natural Science Foundation of China (No. 21775056, 21934002), the National First-class Discipline Program of Food Science and Technology (No. JUFSTR20180301), and the Program of "Collaborative Innovation Center of Food Safety and Quality Control in Jiangsu Province".

Appendix A. Supporting information

Supplementary data associated with this article can be found in the online version at doi:10.1016/j.jhazmat.2021.127353.

References

Abramenko, N., Deyko, G., Abkhalimov, E., Isaeva, V., Pelgunova, L., Krysanov, E., Kustov, L., 2021. Acute toxicity of Cu-MOF nanoparticles (nanoHKUST-1) towards embryos and adult zebrafish. Int. J. Mol. Sci. 22 (11), 5568.

Ansari, M.A., Khan, H.M., Khan, A.A., Cameotra, S.S., Saquib, Q., Musarrat, J., 2014. Interaction of Al_2O_3 nanoparticles with escherichia coli and their cell envelope biomolecules. J. Appl. Microbiol. 116 (4), 772–783.

Aranda, A., Sequedo, L., Tolosa, L., Quintas, G., Burello, E., Castell, J.V., Gombau, L., 2013. Dichloro-dihydro-fluorescein diacetate (DCFH-DA) assay: a quantitative method for oxidative stress assessment of nanoparticle-treated cells. Toxicol. Vitr. 27 (2), 954–963.

Bai, X., Wang, S., Yan, X., Zhou, H., Zhan, J., Liu, S., Sharma, V.K., Jiang, G., Zhu, H., Yan, B., 2020. Regulation of cell uptake and cytotoxicity by nanoparticle core under the controlled shape, size, and surface chemistries. ACS Nano 14 (1), 289–302.

Banerjee, R., Phan, A., Wang, B., Knobler, C., Furukawa, H., Keeffe, M., Yaghi, O.M., 2008. High-throughput synthesis of zeolitic imidazolate frameworks and application to CO_2 capture. Science 319 (5865), 939–943.

Barbul, A., Singh, K., Horev−Azaria, L., Dasgupta, S., Auth, T., Korenstein, R., Gompper, G., 2018. Nanoparticle-decorated erythrocytes reveal that particle size controls the extent of adsorption, cell shape, and cell deformability. ACS Appl. Nano Mater. 1 (8), 3785–3799.

Bharti, B., Meissner, J., Findenegg, G.H., 2011. Aggregation of silica nanoparticles directed by adsorption of lysozyme. Langmuir 27 (16), 9823–9833.

Cai, R., Chen, C., 2018. The crown and the scepter: roles of the protein corona in nanomedicine. Adv. Mater. 31 (45), 1805740.

Cao, M., Cai, R., Zhao, L., Guo, M., Wang, L., Wang, Y., Zhang, L., Wang, X., Yao, H., Xie, C., Cong, Y., Guan, Y., Tao, X., Wang, Y., Xu, S., Liu, Y., Zhao, Y., Chen, C., 2021. Molybdenum derived from nanomaterials incorporates into molybdenum enzymes and affects their activities in vivo. Nat. Nanotechnol. 16 (6), 708–716.

Carrillo, C., Martínez, R., Navarro, M., Pelaz, B., Polo, E., Arenas, A., Olgiati, A., Taboada, P., Soliman, M., Sola, R., Fernandez, S., Catalan, U., Parak, W., Horcajada, P., Álvarez, R., del Pino, P., 2019. Aqueous stable gold nanostar/ZIF-8 nanocomposites for light-triggered release of active cargo inside living cells. Angew. Chem. Int. Ed. 131 (21), 7152–7156.

Chen, T.-T., Yi, J.-T., Zhao, Y.-Y., Chu, X., 2018. Biomineralized metal–organic framework nanoparticles enable intracellular delivery and endo-lysosomal release of native active proteins. J. Am. Chem. Soc. 140 (31), 9912–9920.

Chen, Z.-A., Wu, S.-H., Chen, P., Chen, Y.-P., Mou, C.-Y., 2019. Critical features for mesoporous silica nanoparticles encapsulated into erythrocytes. ACS Appl. Mater. Interfaces 11 (5), 4790–4798.

Daugas, E., Candé, C., Kroemer, G., 2001. Erythrocytes: death of a mummy. Cell Death Differ. 8 (12), 1131–1133.

Deng, S., Yan, X., Xiong, P., Li, G., Ku, T., Liu, N., Liao, C., Jiang, G., 2021. Nanoscale cobalt-based metal-organic framework impairs learning and memory ability without noticeable general toxicity: first in vivo evidence. Sci. Total Environ. 771, 145063.

Deng, X., Liang, S., Cai, X., Huang, S., Cheng, Z., Shi, Y., Pang, M., Ma, P. a, Lin, J., 2019. Yolk–shell structured au nanostar@metal–organic framework for synergistic chemo-photothermal therapy in the second near-infrared window. Nano Lett. 19 (10), 6772–6780.

Dobrovolskaia, M.A., Clogston, J.D., Neun, B.W., Hall, J.B., Patri, A.K., McNeil, S.E., 2008. Method for analysis of nanoparticle hemolytic properties in vitro. Nano Lett. 8 (8), 2180–2187.

Dominguez-Medina, S., Kisley, L., Tauzin, L.J., Hoggard, A., Shuang, B., D. S. Indrasekara, A.S., Chen, S., Wang, L.-Y., Derry, P.J., Liopo, A., Zubarev, E.R., Landes, C.F., Link, S., 2016. Adsorption and unfolding of a single protein triggers nanoparticle aggregation. ACS Nano 10 (2), 2103–2112.

Feng, X., Wu, T., Carreon, M.A., 2016. Synthesis of ZIF-67 and ZIF-8 crystals using DMSO (Dimethyl sulfoxide) as solvent and kinetic transformation studies. J. Cryst. Growth 455, 152–156.

Feng, Y., Wang, H., Zhang, S., Zhao, Y., Gao, J., Zheng, Y., Zhao, P., Zhang, Z., Zaworotko, M.J., Cheng, P., Ma, S., Chen, Y., 2019. Antibodies@MOFs: an in vitro protective coating for preparation and storage of biopharmaceuticals. Adv. Mater. 31 (2), 1805148.

Freund, R., Zaremba, O., Arnauts, G., Ameloot, R., Skorupskii, G., Dincă, M., Bavykina, A., Gascon, J., Ejsmont, A., Gościańska, J., Kalmutzki, M., Lächelt, U., Ploetz, E., Diercks, C., Wuttke, S., 2021. The current status of MOF and COF applications. Angew. Chem. Int. Ed. https://doi.org/10.1002/anie.202106259.

Furukawa, H., Müller, U., Yaghi, O.M., 2015. "Heterogeneity within order" in metal–organic frameworks. Angew. Chem. Int. Ed. 54 (11), 3417–3430.

Gao, P., Chen, Y., Pan, W., Li, N., Liu, Z., Tang, B., 2021. Antitumor agents based on metal–organic frameworks. Angew. Chem. Int. Ed. 60 (31), 16763–16776.

Gao, S., Jin, Y., Ge, K., Li, Z., Liu, H., Dai, X., Zhang, Y., Chen, S., Liang, X., Zhang, J., 2019. Self-supply of O_2 and H_2O_2 by a nanocatalytic medicine to enhance combined chemo/chemodynamic therapy. Adv. Sci. 6 (24), 1902137.

Giardina, B., Messana, I., Scatena, R., Castagnola, M., 1995. The multiple functions of hemoglobin. Crit. Rev. Biochem. Mol. Biol. 30 (3), 165–196.

Gu, Z.-Y., Yang, C.-X., Chang, N., Yan, X.-P., 2012. Metal–organic frameworks for analytical chemistry: from sample collection to chromatographic separation. Acc. Chem. Res. 45 (5), 734–745.

Hao, C., Wu, X., Sun, M., Zhang, H., Yuan, A., Xu, L., Xu, C., Kuang, H., 2019. Chiral core–shell upconversion nanoparticle@MOF nanoassemblies for quantification and bioimaging of reactive oxygen species in vivo. J. Am. Chem. Soc. 141 (49), 19373–19378.

Hao, F., Jing, M., Zhao, X., Liu, R., 2015. Spectroscopy, calorimetry and molecular simulation studies on the interaction of catalase with copper ion. J. Photochem. Photobiol. B Biol. 143, 100–106.

de la Harpe, K.M., Kondiah, P.P.D., Choonara, Y.E., Marimuthu, T., du Toit, L.C., Pillay, V., 2019. The hemocompatibility of nanoparticles: a review of cell–nanoparticle interactions and hemostasis. Cells 8 (10), 1209.

Horcajada, P., Chalati, T., Serre, C., Gillet, B., Sebrie, C., Baati, T., Eubank, J.F., Heurtaux, D., Clayette, P., Kreuz, C., Chang, J.-S., Hwang, Y.K., Marsaud, V., Bories, P.-N., Cynober, L., Gil, S., Férey, G., Couvreur, P., Gref, R., 2010. Porous metal–organic-framework nanoscale carriers as a potential platform for drug delivery and imaging. Nat. Mater. 9 (2), 172–178.

Hu, Y.-J., Liu, Y., Xiao, X.-H., 2009. Investigation of the interaction between berberine and human serum albumin. Biomacromolecules 10 (3), 517–521.

Huang, J., Rauscher, S., Nawrocki, G., Ran, T., Feig, M., de Groot, B.L., Grubmüller, H., MacKerell, A.D., 2017. CHARMM36m: an improved force field for folded and intrinsically disordered proteins. Nat. Methods 14 (1), 71–73.

Jun, C., Xue, Y., Liu, R., Wang, M., 2011. Study on the toxic interaction of methanol, ethanol and propanol against the bovine hemoglobin (BHb) on molecular level. Spectrochim. Acta A Mol. Biomol. Spectrosc. 79 (5), 1406–1410.

Kang, T., Guan, R., Song, Y., Lyu, F., Ye, X., Jiang, H., 2015. Cytotoxicity of zinc oxide nanoparticles and silver nanoparticles in human epithelial colorectal adenocarcinoma cells. LWT Food Sci. Technol. 60 (2, Part 2), 1143–1148.

Kettiger, H., Québatte, G., Perrone, B., Huwyler, J., 2016. Interactions between silica nanoparticles and phospholipid membranes. Biochim. Biophys. Acta 1858 (9), 2163–2170.

Kreno, L.E., Leong, K., Farha, O.K., Allendorf, M., Van Duyne, R.P., Hupp, J.T., 2012. Metal–organic framework materials as chemical sensors. Chem. Rev. 112 (2), 1105–1125.

Kubista, M., Sjöback, R., Eriksson, S., Albinsson, B., 1994. Experimental correction for the inner-filter effect in fluorescence spectra. Analyst 119 (3), 417–419.

Kumar, P., Anand, B., Tsang, Y.F., Kim, K.-H., Khullar, S., Wang, B., 2019. Regeneration, degradation, and toxicity effect of MOFs: opportunities and challenges. Environ. Res. 176, 108488.

Li, H., Eddaoudi, M., O'Keeffe, M., Yaghi, O.M., 1999. Design and synthesis of an exceptionally stable and highly porous metal-organic framework. Nature 402 (6759), 276–279.

Li, Y., Wei, H., Liu, R., 2014. A probe to study the toxic interaction of tartrazine with bovine hemoglobin at the molecular level. Luminescence 29 (2), 195–200.

Lucena, M.A.M., Oliveira, M.F.L., Arouca, A.M., Talhavini, M., Ferreira, E.A., Alves, S., Veiga-Souza, F.H., Weber, I.T., 2017. Application of the metal–organic framework [Eu(BTC)] as a luminescent marker for gunshot residues: a synthesis, characterization, and toxicity study. ACS Appl. Mater. Interfaces 9 (5), 4684–4691.

Ma, Z., Bai, J., Wang, Y., Jiang, X., 2014. Impact of shape and pore size of mesoporous silica nanoparticles on serum protein adsorption and RBCs hemolysis. ACS Appl. Mater. Interfaces 6 (4), 2431–2438.

Mahato, M., Pal, P., Kamilya, T., Sarkar, R., Chaudhuri, A., Talapatra, G.B., 2010. Hemoglobin−silver interaction and bioconjugate formation: a spectroscopic study. J. Phys. Chem. B 114 (20), 7062–7070.

Olson, J.S., Eich, R.F., Smith, L.P., Warren, J.J., Knowles, B.C., 1997. Protein engineering strategies for designing more stable hemoglobin-based blood substitutes. Artif. Cells Blood Substit. Biotechnol. 25 (1–2), 227–241.

Wrobel, T.P., Mateuszuk, L., Chlopicki, S., Malek, K., Baranska, M., 2011. Imaging of lipids in atherosclerotic lesion in aorta from ApoE/LDLR−/− mice by FT-IR spectroscopy and hierarchical cluster analysis. Analyst 136 (24), 5247–5255.

Parikh, S.J., Chorover, J., 2006. ATR-FTIR spectroscopy reveals bond formation during bacterial adhesion to iron oxide. Langmuir 22 (20), 8492–8500.

Park, K.S., Ni, Z., Côté, A.P., Choi, J.Y., Huang, R., Uribe-Romo, F.J., Chae, H.K., O'Keeffe, M., Yaghi, O.M., 2006. Exceptional chemical and thermal stability of zeolitic imidazolate frameworks. Proc. Natl. Acad. Sci. U.S.A. 103 (27), 10186–10191.

Rael, L.T., Ayala-Fierro, F., Bar-Or, R., Carter§, D.E., Barber, D.S., 2006. Interaction of arsine with hemoglobin in arsine-induced hemolysis. Toxicol. Sci. 90 (1), 142–148.

Riccò, R., Liang, W., Li, S., Gassensmith, J.J., Caruso, F., Doonan, C., Falcaro, P., 2018. Metal–organic frameworks for cell and virus biology: a perspective. ACS Nano 12 (1), 13–23.

Ross, P.D., Subramanian, S., 1981. Thermodynamics of protein association reactions: forces contributing to stability. Biochemistry 20 (11), 3096–3102.

Rother, R.P., Bell, L., Hillmen, P., Gladwin, M.T., 2005. The clinical sequelae of intravascular hemolysis and extracellular plasma hemoglobin a novel mechanism of human disease. JAMA 293 (13), 1653–1662.

Ruyra, À., Yazdi, A., Espín, J., Carné-Sánchez, A., Roher, N., Lorenzo, J., Imaz, I., Maspoch, D., 2015. Synthesis, culture medium stability, and in vitro and in vivo zebrafish embryo toxicity of metal–organic framework nanoparticles. Chem. Eur. J. 21 (6), 2508–2518.

Sang, Y., Cao, F., Li, W., Zhang, L., You, Y., Deng, Q., Dong, K., Ren, J., Qu, X., 2020. Bioinspired construction of a nanozyme-based H_2O_2 homeostasis disruptor for intensive chemodynamic therapy. J. Am. Chem. Soc. 142 (11), 5177–5183.

Shao, Q., Wu, P., Gu, P., Xu, X., Zhang, H., Cai, C., 2011. Electrochemical and spectroscopic studies on the conformational structure of hemoglobin assembled on gold nanoparticles. J. Phys. Chem. B 115 (26), 8627–8637.
Simon-Yarza, T., Mielcarek, A., Couvreur, P., Serre, C., 2018. Nanoparticles of metal-organic frameworks: on the road to in vivo efficacy in biomedicine. Adv. Mater. 30 (37), 1707365.
Sovadinova, I., Palermo, E.F., Huang, R., Thoma, L.M., Kuroda, K., 2011. Mechanism of polymer-induced hemolysis: nanosized pore formation and osmotic lysis. Biomacromolecules 12 (1), 260–268.
Tamames-Tabar, C., Cunha, D., Imbuluzqueta, E., Ragon, F., Serre, C., Blanco-Prieto, M. J., Horcajada, P., 2014. Cytotoxicity of nanoscaled metal–organic frameworks. J. Mater. Chem. B 2 (3), 262–271.
Wagner, A., Liu, Q., Rose, O.L., Eden, A., Vijay, A., Rojanasakul, Y., Dinu, C.Z., 2019. Toxicity screening of two prevalent metal organic frameworks for therapeutic use in human lung epithelial cells. Int. J. Nanomed. 14, 7583–7591.
Wang, T., Jiang, X., 2015. Breaking of the phosphodiester bond: a key factor that induces hemolysis. ACS Appl. Mater. Interfaces 7 (1), 129–136.
Wang, X., Wang, X., Wang, M., Zhang, D., Yang, Q., Liu, T., Lei, R., Zhu, S., Zhao, Y., Chen, C., 2018. Probing adsorption behaviors of BSA onto chiral surfaces of nanoparticles. Small 14 (16), 1703982.
Yan, S., Zeng, X., Wang, Y., Liu, B.-F., 2020. Biomineralization of bacteria by a metal–organic framework for therapeutic delivery. Adv. Healthc. Mater. 9 (12), 2000046.
Yang, B., Hao, F., Li, J., Chen, D., Liu, R., 2013. Binding of chrysoidine to catalase: spectroscopy, isothermal titration calorimetry and molecular docking studies. J. Photochem. Photobiol. B Biol. 128, 35–42.
Zhao, X., Hao, F., Lu, D., Liu, W., Zhou, Q., Jiang, G., 2015a. Influence of the surface functional group density on the carbon-nanotube-induced α-chymotrypsin structure and activity alterations. ACS Appl. Mater. Interfaces 7 (33), 18880–18890.
Zhao, X., Lu, D., Hao, F., Liu, R., 2015b. Exploring the diameter and surface dependent conformational changes in carbon nanotube-protein corona and the related cytotoxicity. J. Hazard. Mater. 292, 98–107.
Zhao, X., Lu, D., Liu, S.Q., Li, Y., Feng, R., Hao, F., Qu, G., Zhou, Q., Jiang, G., 2017. Hematological effects of gold nanorods on erythrocytes: hemolysis and hemoglobin conformational and functional changes. Adv. Sci. 4 (12), 1700296.